

Catalysis Science & Technology

Accepted Manuscript



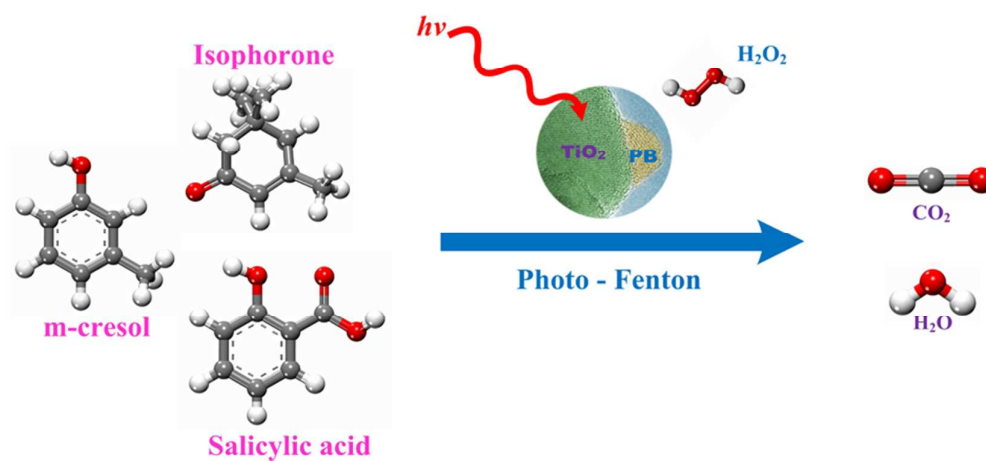
This is an *Accepted Manuscript*, which has been through the Royal Society of Chemistry peer review process and has been accepted for publication.

Accepted Manuscripts are published online shortly after acceptance, before technical editing, formatting and proof reading. Using this free service, authors can make their results available to the community, in citable form, before we publish the edited article. We will replace this *Accepted Manuscript* with the edited and formatted *Advance Article* as soon as it is available.

You can find more information about *Accepted Manuscripts* in the [Information for Authors](#).

Please note that technical editing may introduce minor changes to the text and/or graphics, which may alter content. The journal's standard [Terms & Conditions](#) and the [Ethical guidelines](#) still apply. In no event shall the Royal Society of Chemistry be held responsible for any errors or omissions in this *Accepted Manuscript* or any consequences arising from the use of any information it contains.

Graphical abstract: (maximum size 8cm x 4cm.)



Text: one sentence: (of maximum 20 words, highlighting the novelty of the work.)

The photo-Fenton process of PB/ TiO_2 nanocomposites to degrade various organic pollutants was firstly investigated with Mössbauer spectroscopy and EPR.

Prussian blue/TiO₂ nanocomposites as a heterogeneous photo-Fenton catalyst for degradation of organic pollutants in water

Xuning Li^{a,b}, Junhu Wang^{a,*}, Alexandre I. Rykov^a, Virender K. Sharma^c, Huangzhao Wei^a, Changzi Jin^a, Xin Liu^a, Mingrun Li^a, Songhua Yu^a, Chenglin Sun^a, and Dionysios D. Dionysiou^d

^a *Dalian Institute of Chemical Physics, Chinese Academy of Sciences, 457 Zhongshan Road, Dalian 116023, China*

^b *University of Chinese Academy of Sciences, Beijing 100049, China*

^c *Department of Environmental and Occupational Health, School of Public Health, Texas A&M University, 1266 TAMU, College Station, Texas 77843, USA*

^d *Environmental Engineering and Science Program, Department of Biomedical, Chemical and Environmental Engineering, 705 Engineering Research Center, University of Cincinnati, Cincinnati, OH 45221, USA*

*Corresponding author. Tel: +86-411-84379159; Fax: +86-411-84685940; Email: wangjh@dicp.ac.cn

ABSTRACT

Nowadays, lots of researches focus on accelerating the $\text{Fe}^{\text{II}}/\text{Fe}^{\text{III}}$ redox cycles to increase the pseudo first-order rates of Fenton reaction. Here Prussian blue/titanium dioxide nanocomposites (PB/ TiO_2 NPs) were firstly designed as heterogeneous photo-Fenton catalyst to increase the Fe^{II} recovery in degrading organic contaminants in water. The PB/ TiO_2 NPs were characterized by various analytical techniques to obtain optimum ratio of PB and TiO_2 for efficient degradation of organics. The performance of the catalysts was tested by following the removal of rhodamine B dye, salicylic acid, m-cresol, and isophorone under various conditions (pH, ratios of PB and TiO_2 , H_2O_2 , and temperature). Formation of the intermediates of iron ($\text{Fe}^{\text{II}}/\text{Fe}^{\text{III}}$) in the studied system using Mössbauer spectroscopy was explored for the first time and presents important insights on the relevant catalytic phenomena. The generation of $\bullet\text{OH}$ radicals in the reaction system was identified using electron paramagnetic resonance spectroscopic techniques. Results demonstrated that the developed PB/ TiO_2 NPs were stable and could degrade organic contaminants in water efficiently.

Keywords: Prussian blue/ TiO_2 nanocomposites; Photo-Fenton; Photocatalysis; Synergy; Organic pollutants removal

1. Introduction

Several industrial activities create streams of wastewaters. Often industrial effluents in several countries are not well treated but flow into lakes, rivers, and groundwater reservoirs.¹ Wastewaters contain a wide range of toxic organic compounds of varying concentrations, which have long-term effects on aquatic life and human health.² Furthermore, the use of untreated water is exacerbated by the increasing utilization of renewable freshwater sources for industrial and agricultural activities.^{3,4} The treatment of contaminated water presents an effective strategy to curtail effects to the environment and also to sustain the increasing demand of purified water. Among the various treatment methods, advanced oxidation processes (AOPs) are appealing since they utilize the highly reactive hydroxyl radical ($\bullet\text{OH}$) to degrade organic compounds.^{5,6} Iron-based species can generate $\bullet\text{OH}$ through Fenton and photo-Fenton reactions (reactions 1-3).⁷⁻⁹



Fenton reaction is favorable at pH around 3 and needs a large amount of iron salts for degrading completely the organic contaminants, which limits its use to treat wastewater.¹⁰ Furthermore, the presence of dissolved iron in the effluent and significant generation of ferric oxide sludge during neutralization of the acidic effluents further limit the practice of Fenton reactions in treating contaminated water.

Heterogeneous processes have been proposed to overcome the drawbacks of homogeneous Fenton reactions.¹¹⁻¹³ This paper focuses on the development of a novel heterogeneous photo-Fenton reaction system consisting of nanocomposites in combination with H_2O_2 and UV. The scheme given in Fig. 1 was hypothesized to harvest the advantages of titanium dioxide (TiO_2)

and Prussian blue ($\text{Fe}^{\text{III}}_4[\text{Fe}^{\text{II}}(\text{CN})_6]_3$) nanocomposites (hereafter marked as PB/TiO₂ NPs), which not only absorb light of wavelengths within most of the solar spectrum, but also have the capability to carry electron-transfer process (reaction 4).¹⁴⁻¹⁷



With the addition of H₂O₂, a Fenton reaction process can be performed in which regeneration of Fe(II) can be established at nearly neutral pH (Fig. 1). Furthermore, photo-Fenton reaction using UV light may also increase the efficiency of generating $\bullet\text{OH}$ by two processes: (i) PB captures the conduction band electron and therefore decrease the recombination of electron-hole pair, and (ii) increase the reduction of Fe^{III} to Fe^{II} in PB on the surface of TiO₂, which facilitates the Fenton reaction. The understanding of the generation of $\bullet\text{OH}$ efficiently to degrade organic pollutants effectively was thus the main objective of this paper.

The aims of the paper are to: (i) synthesize and characterize PB/TiO₂ NPs with optimum loading of PB on the surface of TiO₂ nanoparticles by using different surface analytical techniques, (ii) unveil the mechanism of the coupling and explore any synergistic effects of TiO₂ photocatalysis and PB Fenton system mainly by Mössbauer and electron paramagnetic resonance (EPR), (iii) evaluate the catalytic activity of synthesized material based on the scheme given in Fig. 1 in the oxidation of selected organic pollutants (rhodamine B, m-cresol, isophorone, and salicylic acid) under various conditions and examine the roles of different process parameters, and (iv) determine the stability of PB/TiO₂ NPs in the photo-Fenton process.

2. Experimental

2.1. Materials and chemicals

Rhodamine B (RhB) was purchased from Sigma–Aldrich. Isophorone, m-cresol, and salicylic acid were obtained from Tianjin Guangfu fine chemical research institute, China. Ferric chloride, 30% hydrogen peroxide aqueous solution, and potassium ferrocyanide were acquired from Tianjin Kermel Chemical Reagent Co., Ltd, China. Titanium dioxide (P25) was purchased from Evonik Co. (Frankfurt-Main, Germany). All chemicals were used without further purification. Doubly-distilled deionized water was used throughout this study.

2.2. Preparation of PB/TiO₂ NPs

PB/TiO₂ NPs with different loading of PB were synthesized by a simple chemical solution deposition method.¹⁸ Briefly, a ferrocyanide solution (0.03 M) and a TiO₂ solid powder at different stoichiometric molar ratios of PB and TiO₂ were dissolved in 15 mL water, followed by magnetically stirring for 30 min at ambient temperature. In the mixed colloid solution, 15 mL ferric chloride solution (0.04 M) was added slowly with continuous stirring for another 30 min. The colloid solution was aged for at least 12 hours, which resulted in precipitates. Finally, the precipitate was centrifuged and washed with deionized water three times and the resulting product was dried in an oven at 333 K for 12 hours. One ⁵⁷Fe enriched PB (⁵⁷Fe^{III}₄[Fe^{II}(CN)₆]₃)/TiO₂ sample with a molar ratio of 1/60 was prepared by the same method as that used to synthesize the other samples but instead of FeCl₃ solution by using ⁵⁷FeCl₃ stock solution for Mössbauer characterization.

2.3. Characterization of PB/TiO₂ NPs

The powder X-ray diffraction (XRD) patterns were recorded on a PANalytical X'Pert PRO X-ray diffractometer with Cu K α ($\lambda = 0.15406$ nm) radiation and 2θ range from 10° to 80° . The surface morphology and the element distribution were determined by using a Tecnai G² Spirit transmission electron microscopy (TEM) coupled with an energy-dispersive X-ray (EDX) spectrometer at an accelerating voltage of 120 kV. The images of high resolution transmission electron microscopy (HRTEM) were taken on a Tecnai G² F30 S-Twin TEM operating at an accelerating voltage of 300 kV. The UV-vis diffuse reflection spectra were collected using a UV-vis spectrophotometer (V-550, Jasco, Japan).

The room temperature ^{57}Fe Mössbauer spectra of the selected PB/TiO₂ NPs with a molar ratio of 1/60 were recorded under various simulated conditions by using a Topologic 500A spectrometer and a proportional counter. A $^{57}\text{Co}(\text{Rh})$, moving with a constant acceleration mode, was used as the γ -ray radioactive source. The velocity was calibrated by a standard α -iron foil. Fig. S1 shows the Mössbauer measurement setup in this study. A 27 W black light lamp (FPL27BLB, Sankyo Denki, Japan) was added between the γ -ray detector and the PB/TiO₂ sample holder to perform Mössbauer measurements under UV irradiation. The PB/TiO₂ sample was treated by 30% H₂O₂ aqueous solution and/or irradiated by the UV lamp to these *in-situ* Mössbauer measurements, respectively. The spectra were fitted with the appropriate superpositions of Lorentzian lines using the MossWinn 3.0i computer program. In this way, the ^{57}Fe Mössbauer spectral parameters could be determined, including the isomer shift (IS), the electric quadrupole splitting (QS), the full width at half maximum, and the relative resonance areas of the different components of the absorption patterns.

The DMPO (5,5-dimethyl-1-pyrroline-N-oxide) trapped EPR spectra of the selected PB/TiO₂ NPs with a molar ratio of 1/60 were obtained using a Bruker ESR I200 spectrometer at room temperature, which was operated at X-field with a center field at 3350 G and with the sweep width of 100 G. The microwave frequency was 9.405 GHz and the power was 2.979 mW. The sweep time of the signal channel was 81.9 s, with a 10000 gain at the receiver. Before the test, 5 mg of PB/TiO₂ NPs were added into 5 mL diluted H₂O₂ aqueous solution and H₂O₂ ethanol solution ([H₂O₂] = 0.4 M), respectively. After the mixture was prepared, about 100 μL aliquot was taken and injected to 50 μL DMPO (Aladinn, 30 mM freshly diluted by doubly-distilled water on the day of the experiment) immediately. The obtained solution was transferred into an EPR capillary tube (inner diameter: 0.15 mm), which was then fixed in the resonant cavity of the spectrometer. The EPR signal was measured in a time-resolved manner.

2.4. Catalytic activity measurements of PB/TiO₂ NPs

All the experiments were performed in a dark box. The performance of PB/TiO₂ NPs-H₂O₂ system was firstly tested for removal of RhB dye in doubly-distilled water. In all the experiments, 50 mg PB/TiO₂ NPs were added into a 50 mL RhB solution (initial 12 mg L⁻¹) and then stirred in water bath for 30 min at a certain temperature to establish the adsorption/desorption equilibrium. The temperature of the reaction solution was maintained using a temperature-controller water bath. If necessary, the pH of the PB/TiO₂ suspension RhB aqueous solution was adjusted by using either 0.1 M HNO₃ or 0.1 M NaOH aqueous solution. The reaction was initiated by separately adding different amounts of H₂O₂ aqueous solution (simultaneously turning on the lamp for the UV or visible-light irradiation experiments). In the

UV irradiation experiments, the reaction solution was irradiated using a 27 W black light lamp (FPL27BLB, Sankyo Denki, Japan), which emitted light with a peak at 368 nm wavelength. In the visible-light irradiation experiments, the reaction solution was irradiated using a Xenon lamp (MAX-303, Asahi Spectra Co., Ltd), which had a light intensity of 13.3 mW cm^{-2} . Figs. S2 and S3 show the emission spectra of the UV and visible light lamps, respectively. The distance between the lamp and the solution was 15.0 cm. The intensity of the UV light was adjusted to $\sim 2.5 \text{ mW cm}^{-2}$. During the reaction, 2 mL samples were periodically taken out and centrifuged at 12000 rpm before measuring the UV-vis absorption spectra of solutions. The concentration and mineralization of RhB were investigated by UV-vis absorption spectrophotometer (Cintra, GBC, Australia) and total organic carbon analyzer (TOC-VCPH/CPN, Shimadzu, Japan), respectively. There was no considerable RhB adsorption on the surface of PB/TiO₂ NPs. In addition, there was no detectable removal of RhB in the presence of UV irradiation alone. For a comparison, the RhB-H₂O₂ system was also investigated without the addition of PB/TiO₂ NPs using the same procedure.

The performance of PB/TiO₂ NPs-H₂O₂ system was furthermore tested for the removal of three other model organic pollutants, isophorone, m-cresol, and salicylic acid under the selected reaction conditions ([substrate] = 50 mg L⁻¹, [H₂O₂] = 0.4 M, Catalyst = 1.0 g L⁻¹, T = 308 K, and 27 W black light with average 2.5 mW cm^{-2} intensity) following a similar procedure as that used in RhB degradation experiments. Isophorone is used as solvent and chemical intermediate in plastics, pesticides, and pharmaceuticals and is thus found in wastewater. The USA Environmental Protection Agency has classified isophorone as a Group C contaminant, which is a possible human carcinogen.¹⁹ The concentrations of these pollutants in the samples were determined by high performance liquid chromatography (HPLC). The column used was a C18

reverse phase Phenomenex Bondclone (300 x 3.9 mm). The instrument was Perkin-Elmer series 200, USA. The mobile phase was methanol/water mixture at ratios of 70:30, 80:20, 20:80 (V/V) while the detection wavelength was set at 243 nm, 272 nm, and 300 nm for isophorone, m-cresol, and salicylic acid, respectively. The flow rate of the mobile phase was at 1.0 mL min⁻¹.

3. Results and discussion

3.1. Characterization of PB/TiO₂ NPs

Initially, PB/TiO₂ NPs were characterized by XRD analysis as shown in Fig. 2. The observed peaks of (101), (110), (004), (105), and (204) in Fig. 2 correspond to the characteristic peaks of anatase and rutile contained in Evonik P25 while the peaks of (200) and (400) are assigned to PB.²⁰ The intensity of the (200) peak of PB became stronger with the increase in the molar ratios of PB to TiO₂. The XRD results verified the successful synthesis of PB/TiO₂ NPs. The PB/TiO₂ NPs were synthesized under mild acidic solution and therefore the surface of TiO₂ nanoparticles was positively charged ($z_{\text{ipc}} \approx 7.0$),²¹ which could interact with negatively charged cyanoferrate anions ($[\text{Fe}(\text{CN})_6]^{4-}$) to produce PB/TiO₂ NPs.²² It seems that the reaction of Fe³⁺ with $[\text{Fe}(\text{CN})_6]^{4-}$ grafted on the TiO₂ surface led to the formation of PB nanoparticles on the surface of TiO₂. After separation of the blue precipitates by centrifugation, the solution was very clear; indicating that PB and TiO₂ formed compressed composites in the investigated molar ratios of PB and TiO₂ from 1/15 to 1/200.

The morphology, element distribution, and structure of PB/TiO₂ NPs were characterized by TEM-EDX and HRTEM techniques and results are presented in Fig. 3a-g. It could be clearly

seen that the increasing mole ratios of PB increased the content of PB nanoparticles over the surface of TiO₂. Fig. 3g shows the HRTEM image of PB/TiO₂ NPs with a molar ratio of 1/60. The observed lattice fringes of the smaller crystallite correspond to the {002} planes of PB (~0.51 nm).¹⁷ The lattice fringes of the larger particle could be assigned to the {011} planes of anatase in Evonik P25 (~0.35 nm).²³ The HRTEM results demonstrated that well crystallized PB nanoparticles were uniformly dispersed on the surface of TiO₂ nanoparticles and without the formation of thin film; similar to the finding of a previous study.²⁴ The elemental distribution obtained from the EDX spectrum of PB/TiO₂ NPs with a molar ratio of 1/60 as shown in Fig. 3h also supported that PB and TiO₂ coexisted in the PB/TiO₂ NPs.

Furthermore, the UV-vis diffuse reflectance spectra of PB/TiO₂ NPs with different molar ratios were performed as shown in Fig. 4. Pure P25 TiO₂ had only a strong absorption at light wavelength (λ) < 400 nm. New absorption bands of PB nanoparticles appeared between 400 and 800 nm after the formation of P25-PB composites; indicating that the PB/TiO₂ NPs can absorb not only UV light but also visible light and thus they are potential candidate materials for the degradation of organic pollutants using photo-Fenton driven by solar light.

3.2. Reaction mechanism and reactive intermediates

Initially, attempt was made to examine if any change in valence of iron via electron-transfer in the studied heterogeneous system occurred. The ⁵⁷Fe Mössbauer spectroscopy is an ideal method for determining the oxidation state and spin-state of iron ions in a solid. The parameters of the Mössbauer spectroscopy, isomer shift (IS) and quadruple splitting (QS) are listed in Tables 1 and 2. IS is sensitive to the iron valence state while QS varies with the coordination

environment. Fig. 5 shows the Mössbauer spectra of ^{57}Fe enriched $\text{PB}({}^{57}\text{Fe}^{\text{III}}_4[\text{Fe}^{\text{II}}(\text{CN})_6]_3)/\text{TiO}_2$ NPs sample with and without UV irradiation. The ^{57}Fe enrichment into the high-spin site Fe^{III} allowed us to confirm that the UV irradiation had no effect on the values of the hyperfine parameters of this site. This suggests that high-spin Fe^{III} in PB/TiO_2 NPs could not be reduced to high-spin Fe^{II} by photo-induced electrons of TiO_2 . It could be that the electron-transfer in PB/TiO_2 in photo-Fenton process only occurred on the low-spin Fe^{II} .

The electron-transfer in PB/TiO_2 in photo-Fenton process was investigated by carrying out a series of Mössbauer measurements focusing on the low-spin site in non-enriched samples. The low-spin Fe^{II} and Fe^{III} are difficult to distinguish in bulk Prussian blue particles,²⁵ but for the nanoparticles, it was easier because of the large specific surface area and thus more electron-transfer reactions could be happened. Considering that the electron-transfer rate (τ_r) related to Fenton reaction cycle might be in two different regimes with respect to the characteristic time in Mössbauer spectroscopy ($\tau_M \approx 10^{-8}$ s),²⁶ the Mössbauer spectra were analyzed using two models, which are described below.

Model I: slow electron-transfer between low-spin Fe^{II} and Fe^{III} . This model is applicable when the electron-transfer is slower than the characteristic time of Mössbauer spectroscopy. Because the low-spin Fe^{III} has five electrons in the t_{2g} orbital group, it should have some quadruple splitting.²⁷ The finite value of QS originates from the valence electron term if the electron-transfer on the surface of nanoparticle is slower than 10^{-8} s. The spectra with a quadrupole doublet for low-spin Fe^{III} and a singlet for low-spin Fe^{II} are shown in Fig. 6. From this model, we could identify the percentages of low-spin Fe^{III} and Fe^{II} in different reaction conditions. The increase of low-spin Fe^{III} was observed when the reaction with H_2O_2 was conducted, however, after the irradiation by UV lamp, the percentage of low-spin Fe^{III} changed

back to its original value as listed in Table 1. This supports the reduction of low-spin Fe^{III} by the photo-induced electrons of TiO₂, proposed in the scheme given in Fig. 1.

Model II: fast electron-transfer between low-spin Fe^{II} and Fe^{III}. This model is applicable when the electron-transfer is faster than the characteristic time of Mössbauer spectroscopy. The spectra using the model of an average valence was analyzed. In this model, as the electron-transfer was very fast, we describe the state of low-spin iron (average between Fe^{II} and Fe^{III}) by a singlet subspectrum as shown in Fig. 7. Since the crystallographic environments of the low-spin Fe^{II} and Fe^{III} were very similar, the time averaging of the electron density would result in some intermediate value of the isomer shift.²³ The isomer shift of the low-spin mixed-valent state Fe^{II}/Fe^{III} changed from -0.152 mm s⁻¹ to -0.142 mm s⁻¹ when we conducted the *in-situ* reaction with H₂O₂ (Table 2). This may be due to shift of the electron density towards more oxidized state (Fe^{III}).²⁸ After the irradiation by UV lamp, the IS changed to its original value of -0.153 mm s⁻¹. This indicates the shift of the average valence state towards more reduced state (Fe^{II}) owing to the participation of the photo-induced electrons of TiO₂, also supports the reduction of low-spin Fe^{III} by the photo-induced electrons of TiO₂ (see the scheme in Fig. 1).

Formation of •OH in the suggested scheme given in Fig. 1 was explored by EPR technique (Fig. 8). In the PB/TiO₂-H₂O₂ aqueous system, the EPR signal for DMPO-•OH adducts with a spacing of 15 G in magnetic field appeared. The g factor of the signal was 2.0062 and the intensity ratio was 1:2:2:1.²⁹ As •OOH radicals are unstable in aqueous solution, PB/TiO₂-H₂O₂-ethanol system was further used to confirm their formation as shown in Fig. 8.³⁰ There were no six-fold characteristic peak signals of •OOH radicals. The g factor of 2.0060 represents the characteristic of •OH. The slight change of the intensity may be because of the solvent effect. These results confirmed that •OH radicals were the main reactive intermediates.

3.3. Catalytic activity of PB/TiO₂ NPs

A series of experiments were carried out to demonstrate the catalytic activity of PB/TiO₂ NPs with a molar ratio of 1/60 under different conditions as shown in Fig. 9. The removal efficiency of RhB by UV-TiO₂ system was 77.8% in 30 min. A similar efficiency was found in the UV-TiO₂-H₂O₂ system and very low efficiency was found in the UV-H₂O₂ system. The PB/TiO₂ NPs exhibited no significant activity under illumination with UV irradiation. This could be attributed to the partial coverage of TiO₂ by PB. In such composites, PB served as a conductor which could facilitate recombination of holes with the photogenerated electrons on the TiO₂ surface.¹⁵ Interestingly, with the addition of H₂O₂ in the reaction solution of the UV-PB/TiO₂ system, the removal efficiency was clearly enhanced to 95.6% and the corresponding TOC removal efficiency of RhB was 38.5% in 30 min (Fig. S4). This agrees with the increase in efficiency of the generation of [•]OH, based on the proposed scheme 1 given in Fig. 1. Table 3 shows the rate constants (*k*) of photo-Fenton reaction for RhB degradation over PB/TiO₂ NPs under different conditions. The values of *k* were $(5.34 \pm 0.2) \times 10^{-2} \text{ min}^{-1}$ and $(5.20 \pm 0.5) \times 10^{-3} \text{ min}^{-1}$ for PB/TiO₂-H₂O₂ and UV-H₂O₂, respectively. The sum of values of *k* for these two processes is $(5.86 \pm 0.6) \times 10^{-2} \text{ min}^{-1}$, which is smaller than the rate constants for UV-PB/TiO₂-H₂O₂ system ($k = (10.2 \pm 0.2) \times 10^{-2} \text{ min}^{-1}$). These results demonstrate that the synergistic effect exists between photocatalysis and Fenton reactions, furthermore, the Fenton effect gives the dominant contribution for the high removal efficiency of RhB.

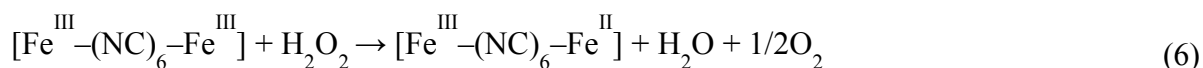
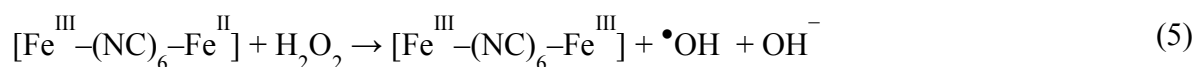
3.4. Synergistic effect of PB/TiO₂ NPs as a heterogeneous photo-Fenton catalyst

In order to evaluate the synergistic effects between photocatalysis and Fenton reactions, PB/TiO₂ NPs with different loading of PB were synthesized and a series of RhB degradation experiments was carried out for comparison. Figs. S5 and S6 show the results on the effect of PB content on the catalytic activity of PB/TiO₂ NPs with or without UV irradiation, respectively. The degradation of RhB followed the pseudo first-order kinetics.³¹ Fig. 10 shows the first-order rate constants of PB/TiO₂ NPs with different molar ratios under different reaction systems. There was no activity of PB/TiO₂ NPs with different molar ratios under UV irradiation without H₂O₂. The reason should be the same as that mentioned above for the PB/TiO₂ NPs with a molar ratio of 1/60. This supports the synergism between the TiO₂ photocatalysis in the photo-Fenton process. With the assistance of UV and H₂O₂, the photo-induced electrons of TiO₂ could reduce the Fe^{III} in PB oxidized by H₂O₂, thus increasing the reaction rate.

The Fenton activity of PB/TiO₂-H₂O₂ increased linearly with the increase of PB loading on the surface of TiO₂. This is because PB (Fe^{III}₄[Fe^{II}(CN)₆]₃) contained Fe^{II}, the activity increased with the increase of iron. However, when the mole ratio of PB/TiO₂ was 1/15, UV light seemed to have no more contribution to the photo-Fenton reaction. This may be explained by considering that high surface coverage of TiO₂ by PB NPs could inhibit penetration of UV light to the surface of TiO₂. In subsequent experiments, the mole ratio of PB/TiO₂ = 1/60 was chosen because it yielded the maximum synergism in the photo-Fenton process.

The steps of oxidation of organic pollutants in water by the photo-Fenton process are described by reactions 5-9. Without the UV irradiation, the reaction between PB and H₂O₂ generates •OH and the Fe^{III} containing species in PB (reaction 5). However, Fe^{III} is further reduced by H₂O₂ to Fe^{II} (reaction 6). This later step regenerates PB for further utilization in the

Fenton reaction. In the presence of UV radiation in the PB/TiO₂-H₂O₂ system, reactions 7-9 also occur, leading to enhanced degradation. UV irradiation of the surface of TiO₂ induces electron and hole pairs (reaction 7). The hole oxidizes the water molecule to produce •OH. Therefore •OH is produced from two reactions (5 and 8) in the photo-Fenton system which results in the increased removal efficiency of RhB compared to that obtained in dark Fenton process. Moreover, the electron induced in reaction 7 can reduce Fe^{III} species in [Fe^{III}-(NC)₆-Fe^{III}] to give back PB (reaction 9). Hence, regeneration of PB is possible from two reactions, 6 and 9, which facilitate the Fenton reaction in the studied system. Reactions 5-9 support the postulated mechanism in the scheme given in Fig. 1.



This synergy between photocatalysis and Fenton reactions was also observed in the studies on the removal of isophorone, m-cresol, and salicylic acid as shown in Fig. 11. Only 15 min were needed to completely oxidize m-cresol and salicylic acid. The removal of these compounds in the photocatalytic system using TiO₂ has been reported previously.^{32, 33} In the studied system, both salicylic acid and m-cresol degraded faster than isophorone. The trend seen in Fig. 11 may be related to the reactivity of the organic compounds with •OH. The reported pseudo second-order rate constants for the reactions of salicylate ion and m-cresol with •OH are $(1.2 - 2.4) \times 10^{10} \text{ M}^{-1} \text{ s}^{-1}$ (pH 7.0).³⁴ However, the rate constant for the reaction of cyclohexene, which contains double

bond like the isophorone molecule, with $\bullet\text{OH}$ is $8.8 \times 10^9 \text{ M}^{-1} \text{ s}^{-1}$ (pH 7.0).

The RhB degradation efficiency of PB/TiO₂ under visible light irradiation was also investigated (Fig. S7). The results clearly suggest that the visible light can also be suitable for degrading RhB using a PB/TiO₂ photocatalyst.

3.5. Factors influencing the degradation of RhB by UV-PB/TiO₂-H₂O₂ process

The effect of pH on the degradation of RhB in the range of 3.0 to 11.0 was examined and results are presented in Fig. 12. The degradation of RhB could be achieved over the entire pH range. This indicates that the PB/TiO₂ NPs could improve the pH effectiveness of the Fenton reaction. There was only decrease $\sim 10\%$ in removal efficiency as pH changed from 3.0 to 10.0. However, the values of k decreased significantly as the solution pH increased to 11.0. Importantly, removal efficiency was reasonably maintainable even when the reaction rate constant decreased from $\sim 23.0 \times 10^{-2} \text{ s}^{-1}$ to $\sim 7.0 \times 10^{-2} \text{ s}^{-1}$. This is important as Fenton process is efficient in the acidic pH of 3.0 - 4.0, but the developed photo-Fenton system was effective even under neutral pH conditions of the water and wastewater. Furthermore, no pH adjustment would be needed in treating the water of varied pH conditions.

Next, the effect of H₂O₂ concentration on the degradation of RhB was investigated and the results are depicted in Fig. 13a. The pseudo first-order rate constants of the photo-Fenton process increased with the increase in the concentration of H₂O₂ (0 - 0.5 M). However, the increase in values of k was initially linear with increase in the concentration of H₂O₂ and when the concentration was more than 0.4 M, an increase in the rate constant did not follow linearity. The optimum H₂O₂ concentration for the photo-Fenton process could be explained by the self-

scavenging effect of hydroxyl radicals by hydrogen peroxide.³⁵ The self-decomposition of hydroxyl radical with itself ($\bullet\text{OH} + \bullet\text{OH} \rightarrow \text{H}_2\text{O}_2$) may also contribute to the photo-Fenton process.

Finally, the effect of the reaction temperature on the degradation of RhB was investigated by varying the temperature from 298 K – 328 K as shown in Fig. 13b. Increase in temperature achieved complete removal of RhB. The plot of $\ln k$ vs. $(1/T)$ gave an activation energy of 58.95 kJ mol^{-1} for the studied photo-Fenton process. This value is higher than the activation energy usually obtained for the photocatalytic processes ($\approx 10 \text{ kJ mol}^{-1}$). This result suggests that the Fenton reactions contribute mostly to the activation energy,^{36,37} however, the contribution from the photocatalytic reaction is minor, which is consistent with the results of the catalytic activity measurements.

3.6. Stability of PB/TiO₂ NPs

The operational stability of PB/TiO₂ NPs was explored by testing the degradation of RhB in consecutive runs as shown in Fig. 14. The result demonstrated the regenerated catalyst under photo-Fenton process exhibited good performance even after a four-cycle run. The slight decrease in the catalytic activity may be because of the adsorption of contaminants on reactive sites of the catalyst and the agglomeration during the centrifugation process.³⁸ Overall, the results of Fig. 14 show that PB/TiO₂ NPs were stable and had good catalytic performance for reuse.

4. Conclusions

PB/TiO₂ NPs with different loading of PB were successfully synthesized. The high photo-Fenton activity for decomposing selected organic pollutants by PB/TiO₂ NPs was investigated for the first time. Series of experiments with different reaction conditions confirmed that weaker acidic conditions were favorable for the photo-Fenton process. The Mössbauer spectra provided evidence that the excited electrons of TiO₂ by UV irradiation could accelerate the cycle of low spin Fe^{III} to Fe^{II} in PB and then led to the higher activity. The EPR demonstrated that the active species •OH were the main reactive intermediate. The removal efficiency of RhB was still as high as 95% even after four-cycle runs. Considering with the stability and a wide working pH range (2-11), the PB/TiO₂ NPs were confirmed to have great potential applications on the degradation of various organic pollutants.

Acknowledgements

This work was supported by the Chinese Academy of Sciences for “100 Talents” Project and the National Natural Science Foundation of China (11079036). This work was also partly supported by the Chinese Academy of Sciences Visiting Professorships for Senior International Scientists, Grant No. 2011T1G15. X. N. Li also thanks Professor Hongxian Han of Dalian Institute of Chemical Physics, Chinese Academy of Sciences for his kind guidance to the EPR sample preparation. Many thanks to the anonymous reviewers who have helped improve this paper. V. K. Sharma acknowledges the support of United States National Science Foundation (CBET 1439314).

References

- 1 R. Ordonez, D. Hermosilla, N. Merayo, A. Gasco, C. Negro, and A. Blanco, *Sep. Purif. Rev.*, 2014, 43, 263.
- 2 R.P. Schwarzenbach, T. Egli, T.B. Hofstetter, U. von Gunten, and B. Wehrli, *Ann. Rev. Environ. Res.*, 2010, 35, 109.
- 3 C.J. Vörösmarty, P.B. McIntyre, M.O. Gessner, D. Dudgeon, A. Prusevich, P. Green, S. Glidden, S.E. Bunn, C.A. Sullivan, C.R. Liermann, and P.M. Davies, *Nature*, 2010, 467, 555.
- 4 J.G. Hering, T.D. Waite, R.G. Luthy, J.E. Drewes, and D.L. Sedlak, *Environ. Sci. Technol.*, 2013, 47, 10721.
- 5 J.J. Pignatello, E. Oliveros, and A. MacKay, *Crit. Rev. Environ. Sci. Technol.*, 2006, 36, 1.
- 6 K.E. O'Shea, and D.D. Dionysiou, *J. Phys. Chem. Lett.*, 2012, 3, 2112.
- 7 S. Enami, Y. Sakamoto, and A.J. Colussi, *Proc. Natl. Acad. Sci. U. S. A.*, 2014, 111, 623.
- 8 J.J. Pignatello, D. Liu, and P. Huston, *Environ. Sci. Technol.*, 1999, 33, 1832.
- 9 N. Klammerth, S. Malato, A. Agüera, A. Fernández-Alba, and G. Mailhot, *Environ. Sci. Technol.*, 2012, 46, 2885.
- 10 M. Su, C. He, V.K. Sharma, M. Abou Asi, D. Xia, X. Li, H. Deng, and Y. Xiong, *J. Hazard. Mater.*, 2012, 211, 95.
- 11 A. Dhakshinamoorthy, S. Navalon, M. Alvaro, and H. Garcia, *ChemSusChem*, 2012, 5, 46.
- 12 Y. Zhong, X. Liang, Z. He, W. Tan, J. Zhu, P. Yuan, R. Zhu, and H. He, *Appl. Catal. B*, 2014, 150, 612.
- 13 J.A. Bañuelos, F.J. Rodríguez, J. Manriquez Rocha, E. Bustos, and A. Rodríguez, J.C. Cruz, L.G. Arriaga, L.A. Godínez, *Environ. Sci. Technol.*, 2013, 47, 7927.
- 14 T. Yamamoto, N. Saso, Y. Umemura, and Y. Einaga, *J. Am. Chem. Soc.*, 2009, 131, 13196.
- 15 S. Liu, S. Cheng, L. Feng, X. Wang, and Z. Chen, *J. Hazard. Mater.*, 2010, 182, 665.

- 16 S.-Q. Liu, S. Cheng, L. Luo, H.-Y. Cheng, S.-J. Wang, S. Lou, *Environ Chem Lett*, 2011 9 31.
- 17 S.-Q. Liu, S. Cheng, L.-R. Feng, X.-M. Wang, Z.-G. Chen, *J. Hazard. Mater.* 2010 182 665.
- 18 K. Szacilowski, W. Macyk, and G. Stochel, *J. Mater. Chem.*, 2006, 16, 4603.
- 19 H. Wei, X. Yan, X. Li, S. He, and C. Sun, *J. Hazard. Mater.*, 2013, 244, 478.
- 20 X. Shen, S. Wu, Y. Liu, K. Wang, Z. Xu, and W. Liu, *J. Colloid Interface Sci.*, 2009, 329, 188.
- 21 D. Gummy, C. Morais, P. Bowen, C. Pulgarin, S. Giraldo, R. Hajdu, and J. Kiwi, *Appl. Catal. B*, 2006, 63, 76.
- 22 K. Szacilowski, and W. Macyk, *Comptes Rendus Chimie*, 2006, 9, 315.
- 23 X. Zhou, T. Shi, J. Wu, and H. Zhou, *Appl. Surf. Sci.*, 2013, 287, 359.
- 24 H. Tada, S. Tsuji, and S. Ito, *J. Colloid Interface Sci.*, 2001, 239, 196.
- 25 L. Samain, F. Grandjean, G.J. Long, P. Martinetto, P. Bordet, and D. Strivay, *J. Phys. Chem. C*, 2013, 117, 9693.
- 26 C.A. Gorski, and M.M. Scherer, *Am. Mineral.*, 2010, 95, 1017.
- 27 P. Gütllich, R. Link, and A. Trautwein, *Mössbauer spectroscopy and transition metal chemistry*, Springer, Berlin, 2011, pp 89-102.
- 28 L. Samain, B. Gilbert, F. Grandjean, G.J. Long, and D. Strivay, *J. Anal. At. Spectrom.*, 2013, 28, 524.
- 29 W. Ma, J. Li, X. Tao, J. He, Y. Xu, J.C. Yu, and J. Zhao, *Angew. Chem. Int.*, 2013, 42, 1029.
- 30 C.C. Chen, X.Z. Li, W.H. Ma, J.C. Zhao, H. Hidaka, and N. Serpone, *J. Phys. Chem. B*, 2002, 106, 318.
- 31 M.-W. Chang, T.-S. Chen, and J.-M. Chern, *Ind. Eng. Chem. Res.*, 2008, 47, 8533.

32 H. Labiadh, T.B. Chaabane, L. Balan, N. Becheik, S. Corbel, G. Medjahdi, and R. Schneider, *Appl. Catal. B*, 2014, 144, 29.

33 R. Poblete, E. Otal, L.F. Vilches, J. Vale, and C. Fernández-Pereira, *Appl. Catal. B*, 2011, 102, 172.

34 National Institute of Science and Technology NDRL/NIST Solution Kinetics Database on the Web. <http://kinetics.nist.gov/solution/>.

35 X. Xue, K. Hanna, and N. Deng, *J. Hazard. Mater.*, 2009, 166, 407.

36 M. Karatas, Y.A. Argun, and M.E. Argun, *J. Ind. Eng. Chem.*, 2012, 18, 1058.

37 S. Su, W. Guo, Y. Leng, C. Yi, Z. Ma, *J. Hazard. Mater.*, 2013, 244, 736.

38 Y. Li, and F.S. Zhang, *Chem. Eng. J.*, 2010, 158, 148.

Figure captions

Fig. 1. Proposed reaction scheme for the degradation of organic pollutants by the PB/TiO₂-UV-H₂O₂ system.

Fig. 2. Right: X-ray diffraction patterns of PB/TiO₂ NPs with different molar ratios; Left: enlarging the intensity change of PB's characteristic peak (200).

Fig. 3. TEM images of PB/TiO₂ NPs with different molar ratios. (a) TiO₂ (P25), (b) PB/TiO₂ = 1/200, (c) PB/TiO₂ = 1/100, (d) PB/TiO₂ = 1/60, (e) PB/TiO₂ = 1/30, (f) PB/TiO₂ = 1/15, (g) HRTEM image of PB/TiO₂ = 1/60, and (h) EDX spectrum of PB/TiO₂ = 1/60.

Fig. 4. UV-vis diffuse reflectance spectra of pure TiO₂ (P25) and PB/TiO₂ NPs with different mole ratios.

Fig. 5. Room temperature ⁵⁷Fe Mössbauer spectra of PB(⁵⁷Fe^{III}₄[Fe^{II}(CN)₆]₃)/TiO₂ with and without UV irradiation. The green and blue solid lines represent the high-spin Fe^{III} components in PB with different coordination environment, respectively. The purple solid line represents the low-spin Fe^{II} component in PB.

Fig. 6. Room temperature ⁵⁷Fe Mössbauer spectra of PB/TiO₂ NPs with a molar ratio of 1/60 at different systems. The green singlet and blue doublet subspectra represent the low-spin Fe^{II} and high-spin Fe^{III} components, and the cyan doublet represents the low-spin Fe^{III} component.

Fig. 7. (a) Room temperature Mössbauer spectrum of PB/TiO₂ with a molar ratio of 1/60. The singlet and doublet subspectra represent the low-spin Fe^{II} and high-spin Fe^{III} components, respectively, and (b) the isomer shifts of low-spin Fe^{II} measured at different systems.

Fig. 8. DMPO trapped EPR spectra of three simulated systems. (a) PB/TiO₂(1/60)-H₂O₂-ethanol system; (b) PB/TiO₂(1/60)-H₂O₂ aqueous system; (c) H₂O₂ aqueous system.

Fig. 9. The catalytic activities of RhB degradation in different systems. Reaction conditions: PB/TiO₂ = 1/60 (if needed), [RhB] = 12 mg L⁻¹, [H₂O₂] = 0.4 M (if needed), catalyst = 1.0 g L⁻¹ (if needed), T = 308 K, and 27 W black light with 2.5 mW cm⁻² intensity (if needed).

Fig. 10. The rate constants of RhB degradation over PB/TiO₂ NPs with different molar ratios in different systems. Reaction conditions: [RhB] = 12 mg L⁻¹, [H₂O₂] = 0.4 M (if needed), catalyst = 1.0 g L⁻¹ (if needed), T = 308 K, and 27 W black light with 2.5 mW cm⁻² intensity (if needed).

Fig. 11. The catalytic activities for the degradation of three kinds of different organic substrates over PB/TiO₂ NPs with a molar ratio of 1/60. Reaction conditions: [substrate] = 50 mg L⁻¹, [H₂O₂] = 0.4 M, catalyst = 1.0 g L⁻¹, T = 308 K, and 27 W black light with 2.5 mW cm⁻² intensity.

Fig. 12. Effect of pH on the rate constant (left) and conversion after 30 min (right) for RhB degradation over PB/TiO₂ NPs with a molar ratio of 1/60 under UV irradiation. Reaction conditions: [RhB] = 12 mg L⁻¹, [H₂O₂] = 0.4 M, catalyst = 1.0 g L⁻¹, T = 308 K, and 27 W black light with 2.5 mW cm⁻² intensity.

Fig. 13. Effect of (a) H₂O₂ concentration at 308 K and (b) temperatures between 298 K to 328 K on the rate constant of photo-Fenton reaction for RhB degradation over PB/TiO₂ NPs with a molar ratio of 1/60 under UV irradiation. Reaction conditions: [RhB] = 12 mg L⁻¹, catalyst = 1.0 g L⁻¹, and 27 W black light with 2.5 mW cm⁻² intensity.

Fig. 14. Consecutive runs of the catalytic activities of PB/TiO₂ NPs with a molar ratio of 1/60 for RhB degradation under UV irradiation. Reaction conditions: [RhB] = 12 mg L⁻¹, [H₂O₂] = 0.4 M, catalyst = 1.0 g L⁻¹, T = 318 K, and 27 W black light with 2.5 mW cm⁻² intensity.

Table 1. Room temperature ^{57}Fe Mössbauer parameters of different simulated systems obtained by Model I.

Table 2. Room temperature ^{57}Fe Mössbauer parameters of different simulated systems obtained by Model II.

Table 3. The rate constant of photo-Fenton reaction for RhB degradation over PB/TiO₂ NPs under different conditions.

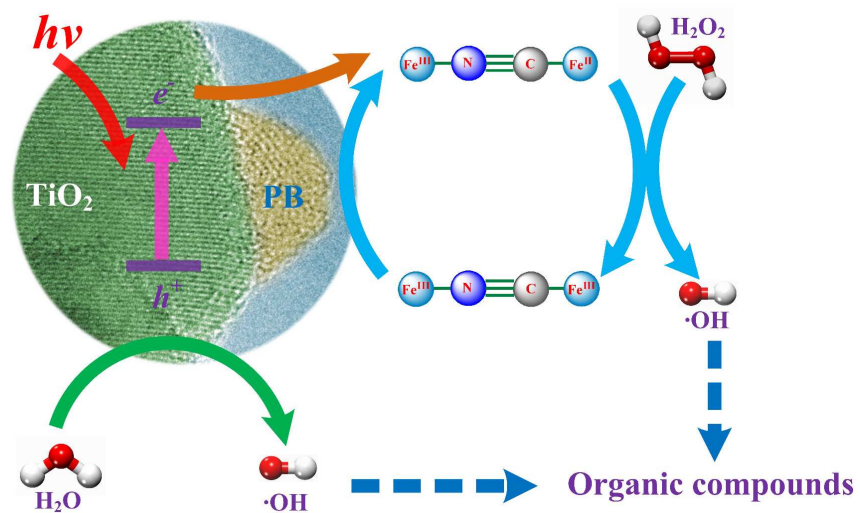


Fig. 1. Proposed reaction scheme for the degradation of organic pollutants by the PB/TiO₂-UV-H₂O₂ system.

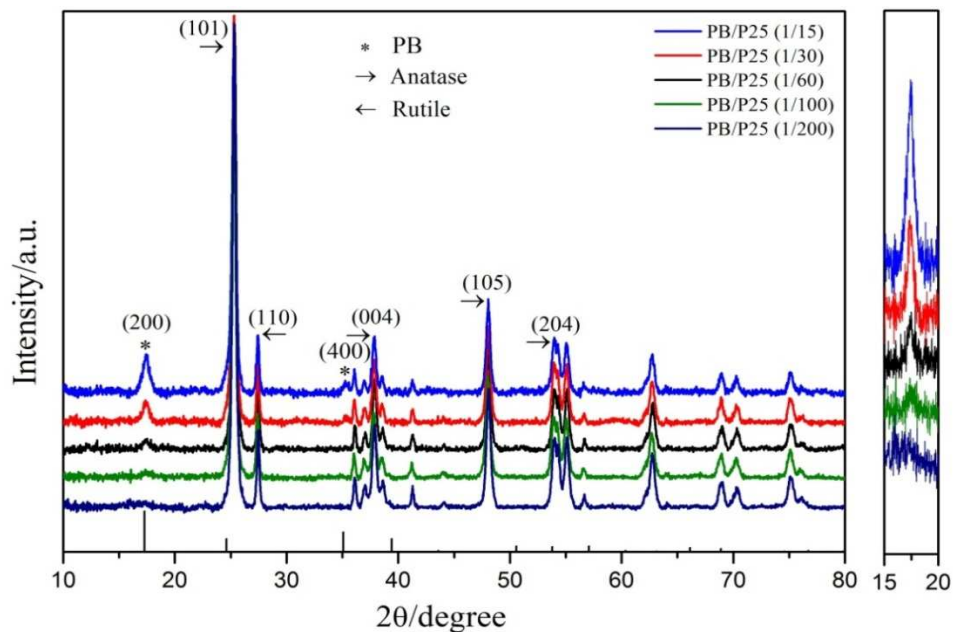


Fig. 2. Right: X-ray diffraction patterns of PB/TiO₂ NPs with different molar ratios; Left: enlarging the intensity change of PB's characteristic peak (200).

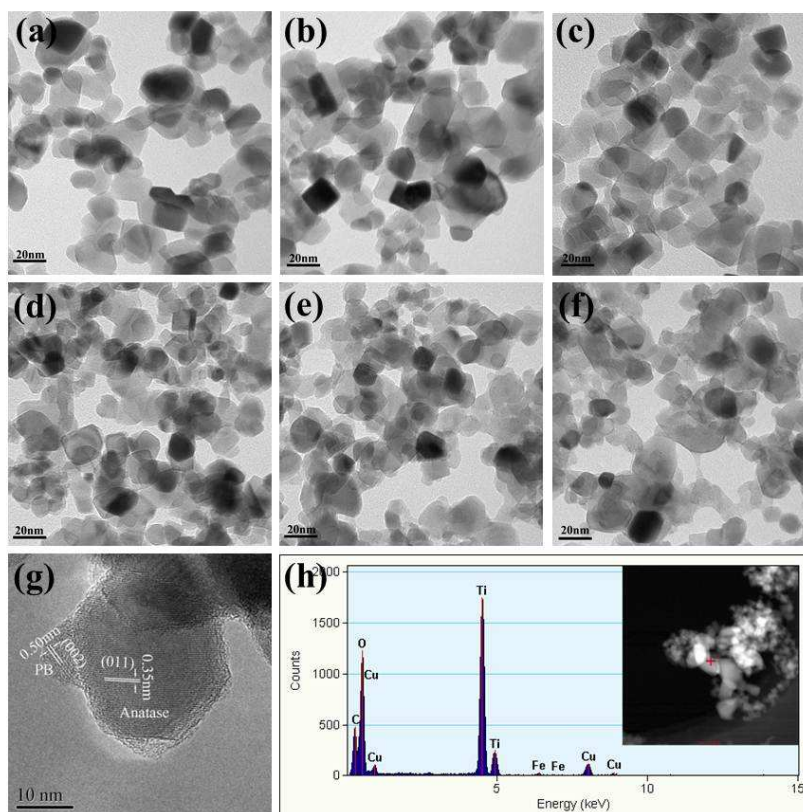


Fig. 3. TEM images of PB/TiO₂ NPs with different molar ratios. (a) TiO₂ (P25), (b) PB/TiO₂ = 1/200, (c) PB/TiO₂ = 1/100, (d) PB/TiO₂ = 1/60, (e) PB/TiO₂ = 1/30, (f) PB/TiO₂ = 1/15, (g) HRTEM image of PB/TiO₂ = 1/60, and (h) EDX spectrum of PB/TiO₂ = 1/60.

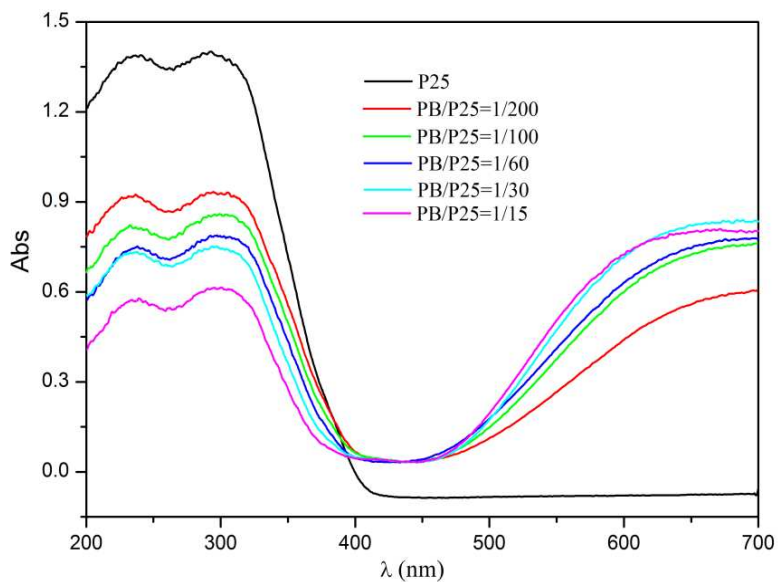


Fig. 4. UV-vis diffuse reflectance spectra of pure TiO_2 (P25) and PB/ TiO_2 NPs with different molar ratios.

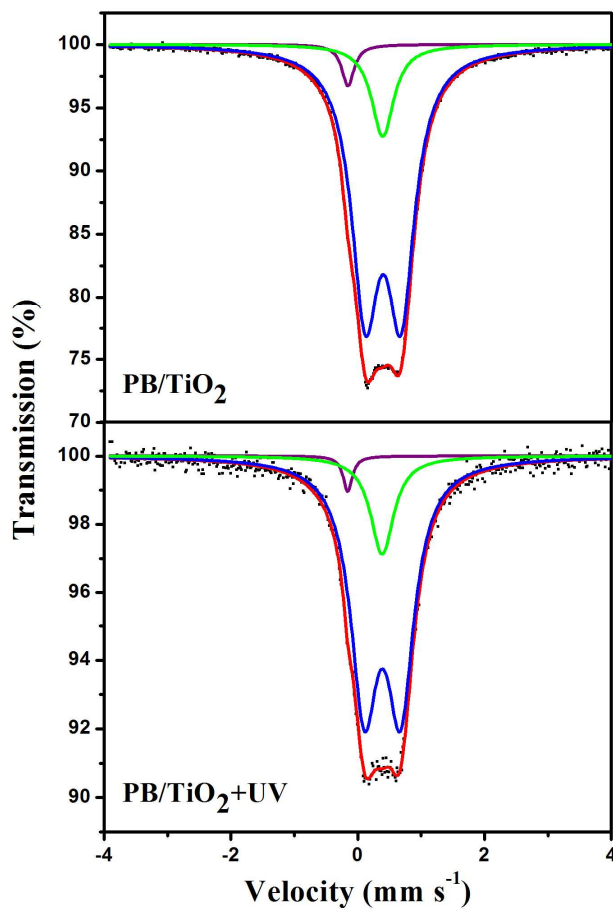


Fig. 5. Room temperature ^{57}Fe Mössbauer spectra of $\text{PB}({}^{57}\text{Fe}^{\text{III}}_4[\text{Fe}^{\text{II}}(\text{CN})_6]_3)/\text{TiO}_2$ with and without UV irradiation. The green and blue solid lines represent the high-spin Fe^{III} component in PB with different coordination environment, respectively. The purple solid line represents the low-spin Fe^{II} component in PB.

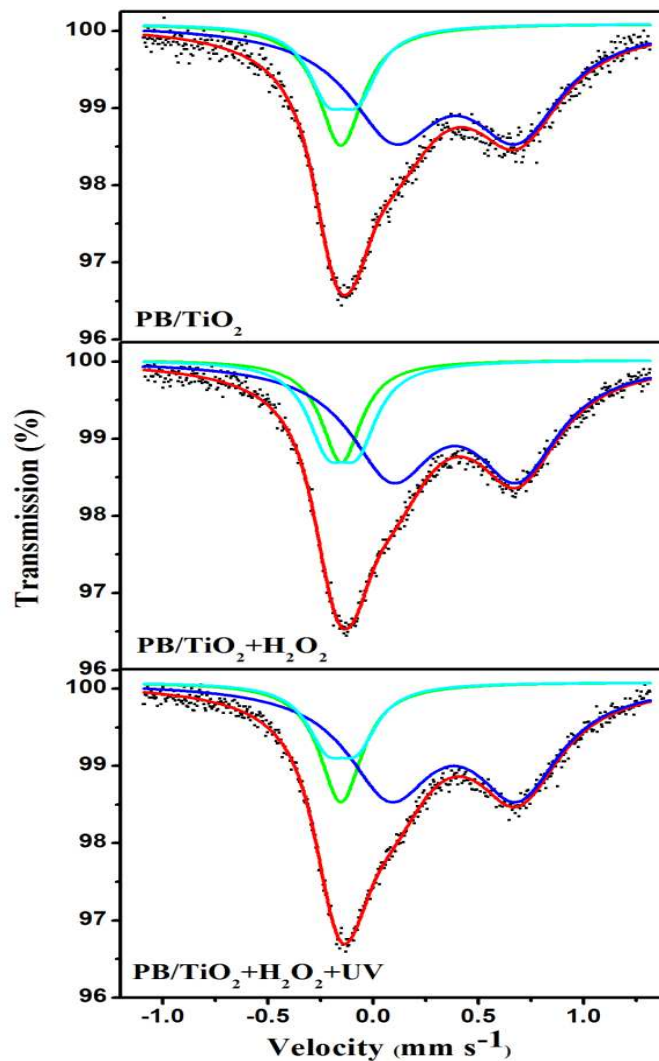


Fig. 6. Room temperature ⁵⁷Fe Mössbauer spectra of PB/TiO₂ NPs with a molar ratio of 1/60 at different systems. The green singlet and blue doublet subspectra represent the low-spin Fe^{II} and high-spin Fe^{III} components, and the cyan doublet represents the low-spin Fe^{III} component.

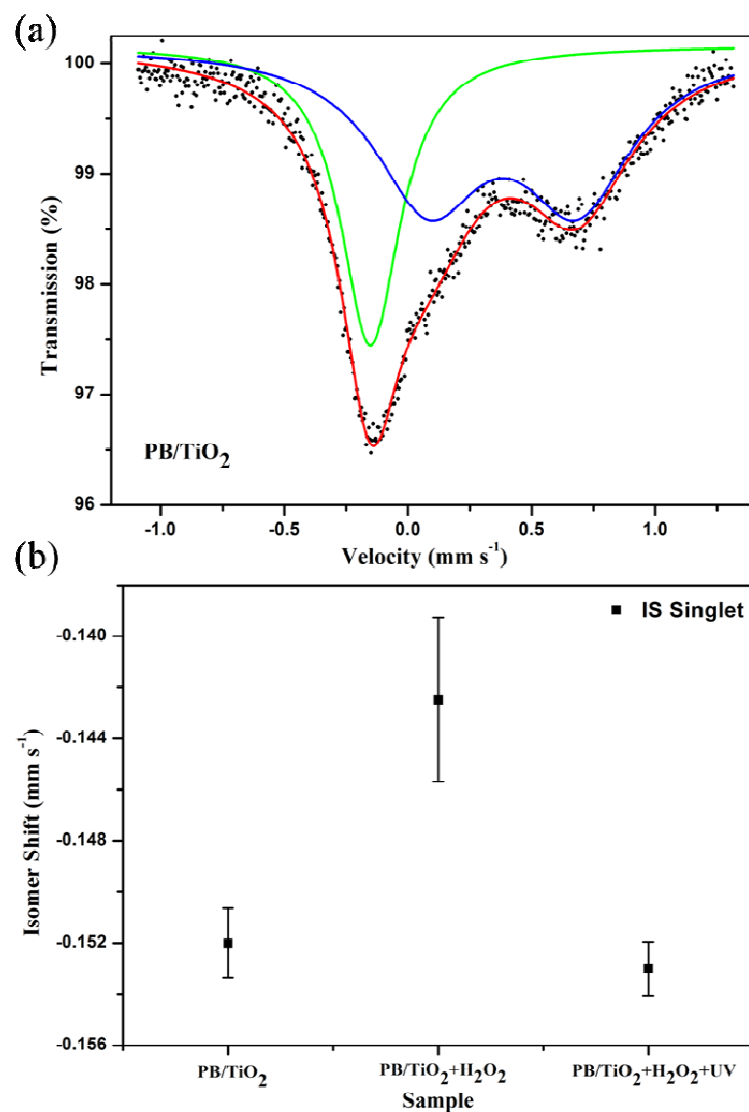


Fig. 7. (a) Room temperature Mössbauer spectrum of PB/TiO₂ with a molar ratio of 1/60. The singlet and doublet subspectra represent the low-spin Fe^{II} and high-spin Fe^{III} components, respectively, and (b) the isomer shifts of low-spin Fe^{II} measured at different systems.

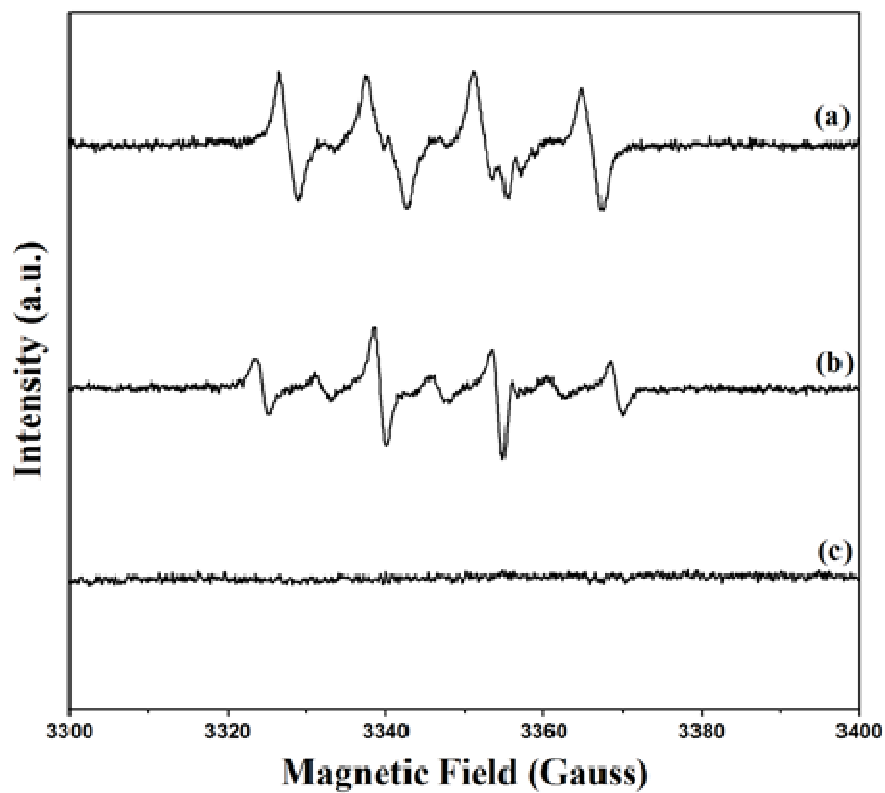


Fig. 8. DMPO trapped EPR spectra of three simulated systems. (a) PB/TiO₂(1/60)-H₂O₂-ethanol system; (b) PB/TiO₂(1/60)-H₂O₂ aqueous system; (c) H₂O₂ aqueous system.

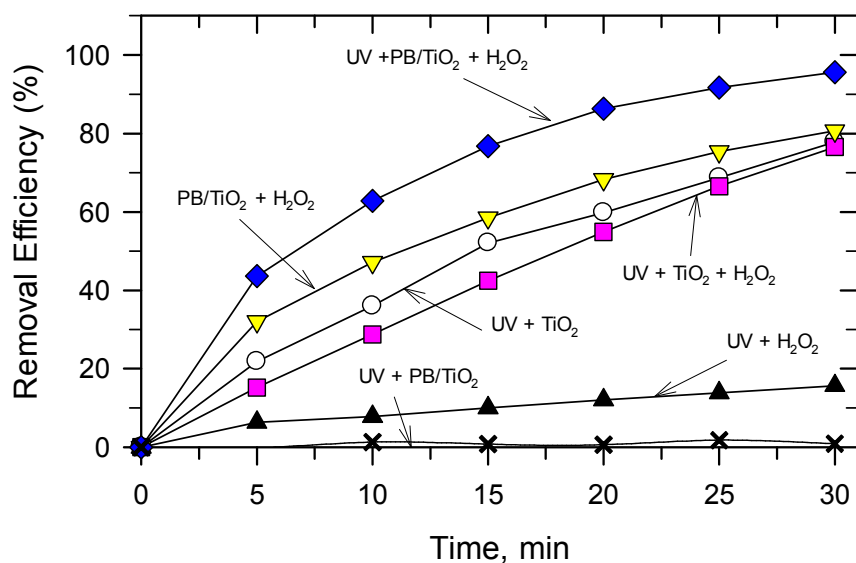


Fig. 9. The catalytic activities of RhB dye degradation in different systems. Reaction conditions: PB/TiO₂ = 1/60 (if needed), [RhB] = 12 mg L⁻¹, [H₂O₂] = 0.4 M (if needed), catalyst = 1.0 g L⁻¹ (if needed), T = 308 K, and 27 W black light with 2.5 mW cm⁻² intensity (if needed).

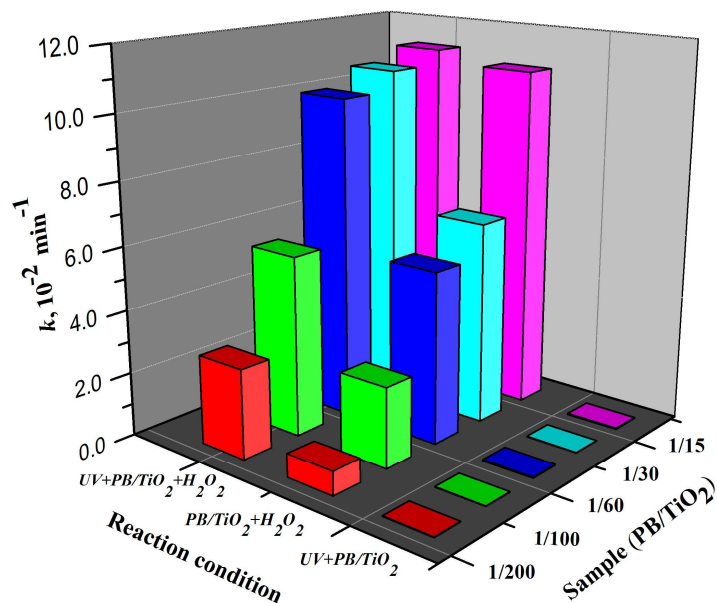


Fig. 10. The rate constants of the RhB degradation over PB/TiO₂ NPs with different molar ratios in different systems. Reaction conditions: [RhB] = 12 mg L⁻¹, [H₂O₂] = 0.4 M (if needed), catalyst = 1.0 g L⁻¹ (if needed), T = 308 K, and 27 W black light with 2.5 mW cm⁻² intensity (if needed).

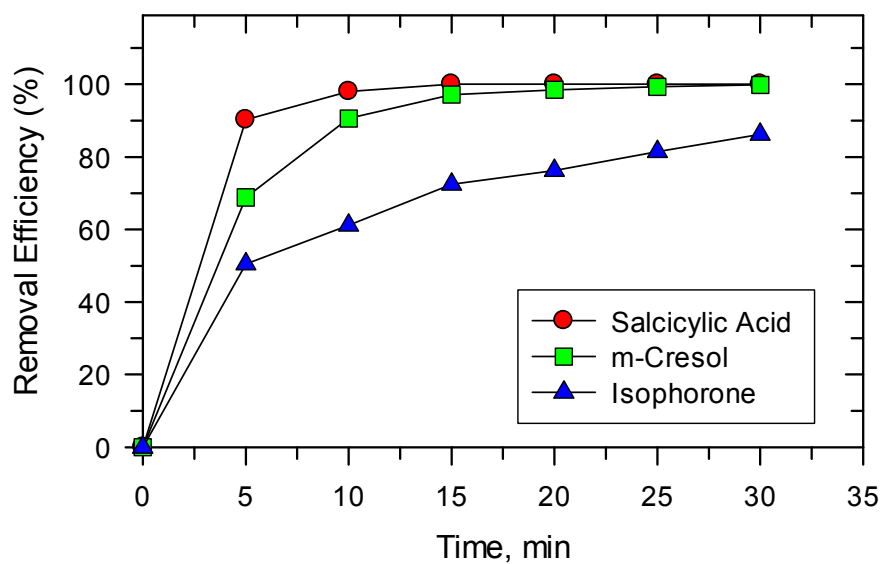


Fig. 11. The catalytic activities for the degradation of three kinds of different organic substrates over PB/TiO₂ NPs with a molar ratio of 1/60. Reaction conditions: [substrate] = 50 mg L⁻¹, [H₂O₂] = 0.4 M, catalyst = 1.0 g L⁻¹, T = 308 K, and 27 W black light with 2.5 mW cm⁻² intensity.

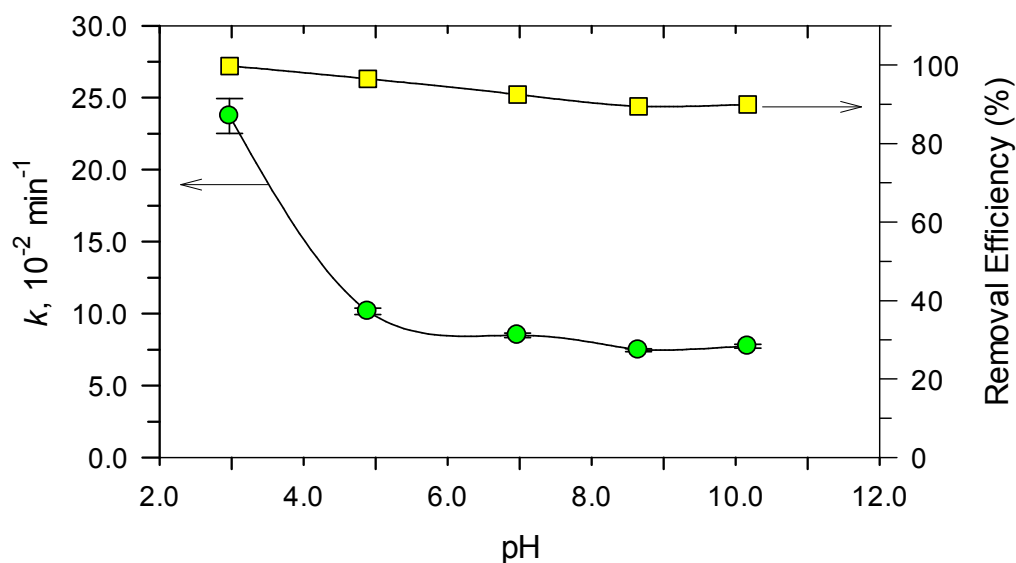


Fig. 12. Effect of pH on the rate constant (left) and conversion after 30 min (right) for RhB degradation over PB/TiO₂ NPs with a molar ratio of 1/60 under UV irradiation. Reaction conditions: [RhB] = 12 mg L⁻¹, [H₂O₂] = 0.4 M, catalyst = 1.0 g L⁻¹, T = 308 K, and 27 W black light with 2.5 mW cm⁻² intensity.

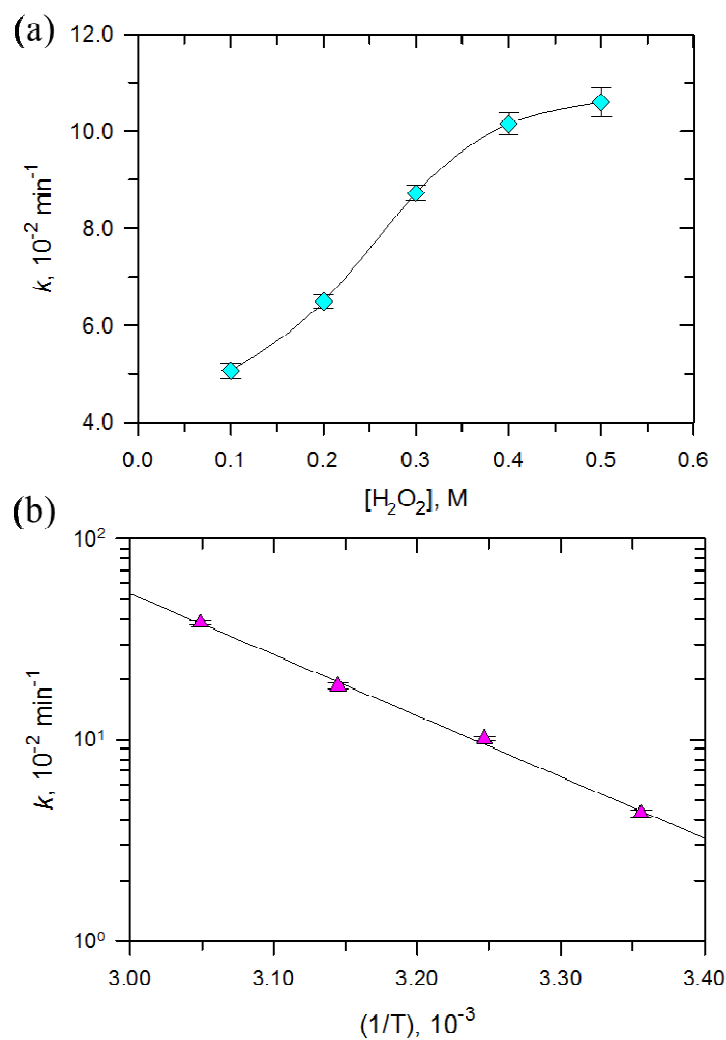


Fig. 13. Effect of (a) H_2O_2 concentration at 308 K and (b) temperatures between 298 K to 328 K on the rate constant of photo-Fenton reaction for RhB degradation over PB/TiO₂ NPs with a molar ratio of 1/60 under UV irradiation. Reaction conditions: $[\text{RhB}] = 12 \text{ mg L}^{-1}$, catalyst = 1.0 g L^{-1} , and 27 W black light with 2.5 mW cm^{-2} intensity.

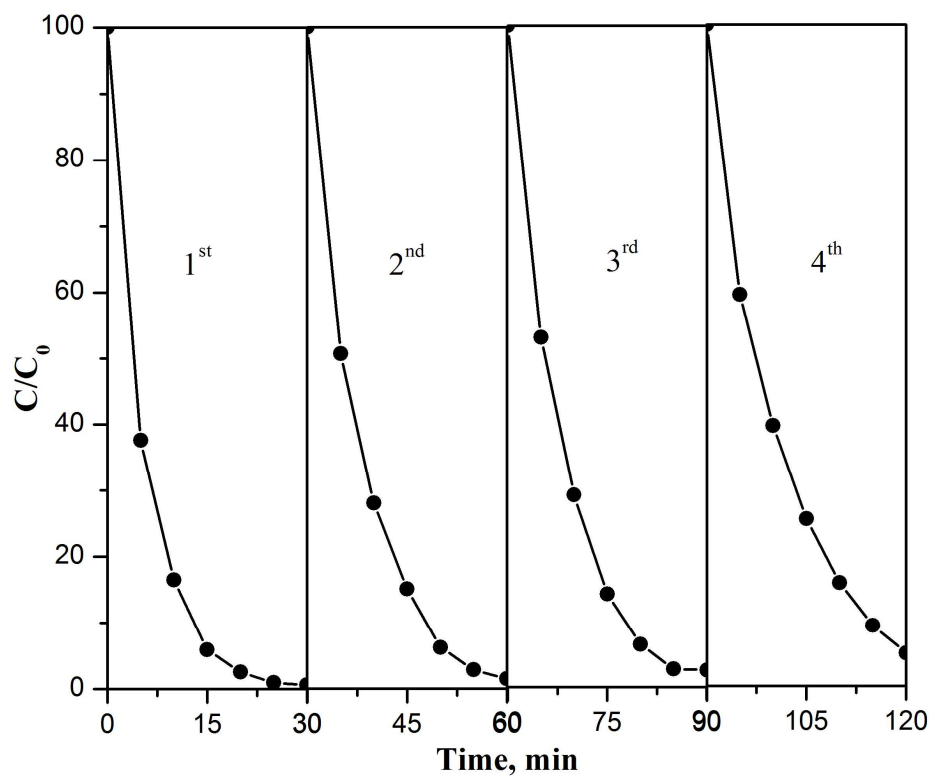


Fig. 14. Consecutive runs of the catalytic activities of PB/TiO₂ NPs with a molar ratio of 1/60 for RhB degradation under UV irradiation. Reaction conditions: [RhB] = 12 mg L⁻¹, [H₂O₂] = 0.4 M, catalyst = 1.0 g L⁻¹, T = 318 K, and 27 W black light with 2.5 mW cm⁻² intensity.

Table 1. Room temperature ^{57}Fe Mössbauer parameters of different simulated systems obtained by Model I

System	Component	IS (mm s^{-1})	QS (mm s^{-1})	Area (%)
PB/TiO ₂	LS Fe ^{II}	-0.152		19
	LS Fe ^{III}	-0.143	0.144	16
	HS Fe ^{III}	0.393	0.583	65
PB/TiO ₂ +H ₂ O ₂	LS Fe ^{II}	-0.152		15
	LS Fe ^{III}	-0.147	0.144	20
	HS Fe ^{III}	0.387	0.595	65
PB/TiO ₂ +H ₂ O ₂ +UV	LS Fe ^{II}	-0.154		19
	LS Fe ^{III}	-0.149	0.144	15
	HS Fe ^{III}	0.383	0.606	66

Experimental errors are $\pm 0.001 \text{ mm s}^{-1}$ for isomer shift (IS), $\pm 0.005 \text{ mm s}^{-1}$ for quadrupole splitting (QS) and 1% for relative area. IS is relative to α -iron foil.

Table 2. Room temperature ^{57}Fe Mössbauer parameters of different simulated systems by Model II

System	Component	IS (mm s^{-1})	QS (mm s^{-1})	Area (%)
PB/TiO ₂	LS Fe ^{II/III}	-0.152		35
	HS Fe ^{III}	0.384	0.602	65
PB/TiO ₂ +H ₂ O ₂	LS Fe ^{II/III}	-0.142		35
	HS Fe ^{III}	0.389	0.565	65
PB/TiO ₂ +H ₂ O ₂ +UV	LS Fe ^{II/III}	-0.153		34
	HS Fe ^{III}	0.377	0.621	66
(^{57}Fe) PB/TiO ₂	LS Fe ^{II}	0.363		16
	HS Fe ^{III}	0.373	0.59	84
(^{57}Fe) PB/TiO ₂ +UV	LS Fe ^{II}	0.362		17
	HS Fe ^{III}	0.366	0.598	83

Experimental errors are $\pm 0.001 \text{ mm s}^{-1}$ for isomer shift (IS), $\pm 0.005 \text{ mm s}^{-1}$ for quadrupole splitting (QS) and 1% for relative area. IS is relative to α -iron foil.

Table 3. The rate constant of photo-Fenton reaction for RhB degradation over PB/TiO₂ NPs under different conditions

System	k, min^{-1}	r^2
UV + PB/TiO ₂ (1/60) + H ₂ O ₂	$(10.2 \pm 0.2) \times 10^{-2}$	0.997
UV + TiO ₂ + H ₂ O ₂	$(4.76 \pm 0.30) \times 10^{-2}$	0.980
UV + TiO ₂	$(4.87 \pm 0.16) \times 10^{-2}$	0.995
PB/TiO ₂ (1/60) + H ₂ O ₂	$(5.34 \pm 0.16) \times 10^{-2}$	0.995
UV + H ₂ O ₂	$(5.20 \pm 0.50) \times 10^{-3}$	0.953
UV + PB/TiO ₂ (1/60)	$(4.00 \pm 2.00) \times 10^{-4}$	0.439